Journal of Advanced Ceramics
先进陶瓷
ISSN 2226-4108
CN 10-1154/TQ
清华大学出版社 Tsinghua University Press
SciOpen

J Adv Ceram 2026, **15**: 9221363

https://doi.org/10.26599/JAC.2026.9221363

Research Article

Near-zero hysteresis in $BaTiO_3$-based piezoceramic enabled by non-freezing high-active glassy polar nanoregions

Hongbo Li[1], Yuhan Luan[2], Rongchuan He[1], Xudong Luo[1], Xu Li[3], Xiaoqiang Song[4], Qingquan Xiao[1], Li Zhang[1], Jiajun Ma[1], An Xue[5,*], Guifen Fan[2,*], Dawei Wang[6,*], Fangfang Zeng[1,*]

[1]*College of Big Data and Information Engineering, Guizhou University, Guiyang 550025, China.*

[2]*School of Optical and Electronic Information, Huazhong University of Science and Technology, Wuhan 430074, China.*

[3]*College of Materials Science and Engineering, Guilin University of Technology, Guilin 541004, China.*

[4]*Zhejiang Key Laboratory of Electronic Functional Ceramics and Devices, Advanced Manufacturing Institute of Huazhong University of Science and Technology, Wenzhou*

325035, China.

[5]School of Materials and Architectural Engineering, Guizhou Normal University, Guiyang 550025, China.

[6]School of Instrumentation Science and Engineering, Harbin Institute of Technology, Harbin 150001, China.

*Corresponding author.

E-mail: A. Xue, xuean1129@163.com;

G. Fan, Fan_gf@mail.hust.edu.cn;

D. Wang, wangdawei102@gmail.com;

F. Zeng, ffzeng@gzu.edu.cn

Received: June 23, 2026; Revised: August 5, 2026; Accepted: August 24, 2026

Abstract: Near-zero strain hysteresis is critical for the performance and reliability of electromechanical devices, yet its realization in environmentally friendly piezoelectric ceramics remains a challenge. Although defect engineering, phase boundary engineering, and the construction of polar nanoregions (PNRs) have been widely

explored to reduce strain hysteresis, these individual approaches have yet to achieve significant improvements. Herein, we propose an effective strategy to engineer high-active glassy polar nanoregions (HAG-PNRs) and defect dipoles in $Ba_{(1-x)}(Sn_{0.11}Ti_{0.89})O_3-0.5xSb_2O_3$ ceramics with multiphase coexistence. By reducing the domain switching energy barrier and frictional damping in piezoelectric ceramics, an ultra-low strain hysteresis (~1.25%) is achieved, representing one of the lowest strain hysteresis values reported in ceramic systems to date. This work offers a novel design paradigm for developing $BaTiO_3$-based lead-free piezoceramics with near-zero strain hysteresis through the controlled formation of HAG-PNRs.

Keywords: high-active glassy polar nanoregions; defects; multiphase coexistence; damping; strain hysteresis

1. Introduction

As materials capable of mutual conversion between mechanical and electrical energy, piezoelectric ceramics have attracted considerable attention for applications in actuators, sensors, and beyond [1−5]. Among the most promising lead-free perovskite materials, barium titanate (BT)-based ceramics have attracted widespread attention [6−8]. However, their large strain hysteresis (H_s; H_s > 20%) limits their application in high-precision actuators [9−14]. Therefore, one of the key challenges in developing BT-based lead-free ceramic materials is how to tailor near-zero H_s. Currently, various strategies have been employed to mitigate H_s [15−21]. For example, Yang et al. established polar nanoregions (PNRs) in $(Ba_{1-x}Sm_x)(Sn_{0.08}Ti_{0.92})O_3$−0.6 wt% MnO_2,

compositions by regulating the configuration and scale of local ferroelectric domains, reducing the H_s to approximately 25% [15]. Li et al. modulated the domain switching barrier in $(Ba_{0.865}Ca_{0.135})(Ti_{0.91}Zr_{0.09})O_3$ via defect engineering, enabling a low H_s of ~20%. Although defect engineering can build an internal electric field to modulate domain wall motion, it pins domain walls, leaving the H_s still relatively high [16]. Baraskar et al. constructed multiphase-coexisting $(Ba_{0.7}Ca_{0.3})(Ti_{0.9}Sn_{0.1})O_3$ ceramic compositions by site engineering. Even though the multiphase coexistence has reduced the switching damping of polar regions, the H_s is as high as ~15% [17]. Nevertheless, these single strategies fail to substantially reduce H_s. Therefore, there is an urgent need to develop lead-free piezoelectric ceramic compositions with low H_s.

In recent years, the ferroelectric glassy state has garnered considerable attention as an emerging concept in the piezoelectric field. This glassy state is characterized by long-range disorder and short-range order, lacking a complete crystal lattice and being free from crystalline defects such as grain boundaries and dislocations, thus exhibiting distinctly different properties from its crystalline counterpart [22]. By tailoring the defect concentration in ceramic systems, the long-range ferroelectric order within the ceramic composition can be disrupted, leaving only dynamic, isolated PNRs, thereby constructing a non-frozen ferroelectric glassy state composition [23]. Simultaneously, by tuning the Curie temperature to below room temperature, the PNRs existing in this state become high-active glassy polar nanoregions (HAG-PNRs). These high-active PNRs differ significantly from ordinary PNRs in dynamics and functional advantages. First, HAG-PNRs lie above the temperature of the maximum dielectric permittivity

(T_m); therefore, they respond much more rapidly to external stimuli. In contrast, ordinary PNRs are located below room temperature and are typically classified, with respect to the freezing temperature, as either non-ergodic or ergodic relaxor states, exhibiting poor reversibility after polarization switching and thus large hysteresis. Moreover, both types of PNRs originate from the disruption of long-range ferroelectric order.

In this work, by deliberately constructing A-site vacancy defects and B-site acceptor doping defects, HAG-PNRs with multiphase coexistence were successfully built in $Ba_{(1-x)}(Sn_{0.11}Ti_{0.89})O_3-0.5xSb_2O_3$ ceramics, yielding a near-zero H_s of ~1.25%. Figs. 1(a) and 1(b) illustrate the evolution of the crystal structure during the process of defect construction. The synergistic effect of HAG-PNRs and multiphase coexistence reduces H_s by lowering the domain switching energy barrier and frictional damping, while defect engineering introduces a built-in electric field that gives rise to asymmetric strain curves. Together, these three factors enable a near-zero H_s under forward electric fields. This work offers a viable pathway for developing ultra-low H_s lead-free compositions.

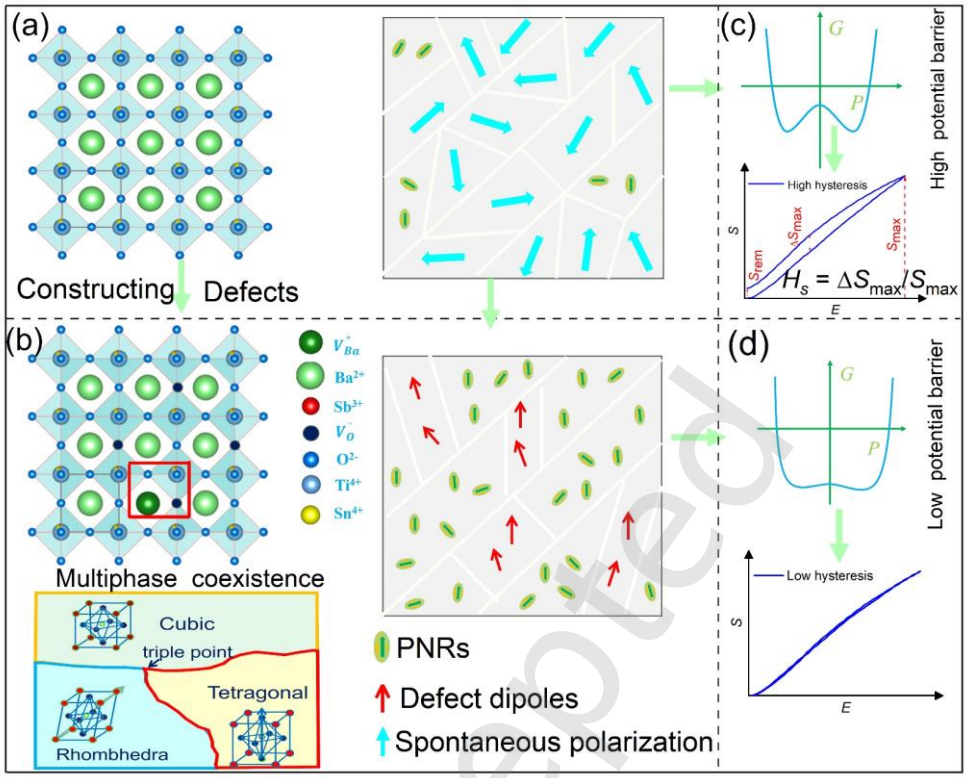

Fig. 1 Schematic illustrations: (a) Crystal structure and domain diagram of the pristine sample. (b) crystal structure, domain diagram and phase structure of $B_{(1-x)}ST-xSb$. (c) high potential barrier and high hysteresis loop. (d) low potential barrier and low hysteresis loops.

2. Experimental methods

$Ba_{(1-x)}(Sn_{0.11}Ti_{0.89})O_3-0.5xSb_2O_3$ (abbreviated as $B_{(1-x)}ST-xSb$, x = 0.005, 0.008, 0.01, 0.03, and 0.05) ceramics were fabricated via the conventional solid−state reaction method. $BaCO_3$ (99%), TiO_2 (99%), SnO_2 (99.5%) and Sb_2O_3 (99.5%) were used as raw materials, and these materials were mixed according to the stoichiometric ratio and ball-milled for 12 hours, and then sieved, dried, and calcined at 1423 K for 3 hours. A second ball-milling, drying, and sieving process was then performed. The resulting powders were mixed with 10 wt% polyvinyl alcohol (PVA) binder, then pressed into disks with a diameter of 10 mm and a thickness of 1 mm. Finally, the obtained pellets

were sintered at 1673 K in air for 4 h. After poling under a DC voltage of 2 kV, the samples were aged for 15 days before the strain measurements were performed. And the strain hysteresis was evaluated using the formula $H_s = \Delta S_{max}/S_{max}$.

The phase structure of the $B_{(1-x)}ST-xSb$ was characterized by X-ray diffraction (XRD) with Cu K-α radiation and Rietveld refinement was performed using the GSAS−II software (version SVN5799). Raman spectra were collected using a Raman spectrometer (Labram HR Evolution, HORIBA S.A.S.), and Raman fitting was performed using the LabSpec software. The surface morphology of the materials was characterized by scanning electron microscope (SEM; JSM-6700F, JEOL, Japan). Dielectric properties were measured using a precision impedance analyzer (HP 4294A, Agilent, USA) at various frequencies (100 Hz, 1 kHz, 10 kHz, and 100 kHz). The polarization–electric field intensity (*P*−*E*) and current–electric field hysteresis loops (*I*−*E*) of the samples were measured at room temperature using a ferroelectric analyzer (FETS-2000, Wuhan Yanhe Science and Technology Co., Ltd., China). The Strain–Electric field curve (*S*–*E*) were measured using an aixACCT TF Analyzer 2000 E. PFM measurements were performed using piezoresponse force microscopy (PFM; MFP-3D, Asylum Research, Oxford Instruments, USA), and transmission electron microscopy (TEM; F20, FEI, USA) was used for microstructural observation and selected area electron diffraction (SAED).

3. Results and discussion

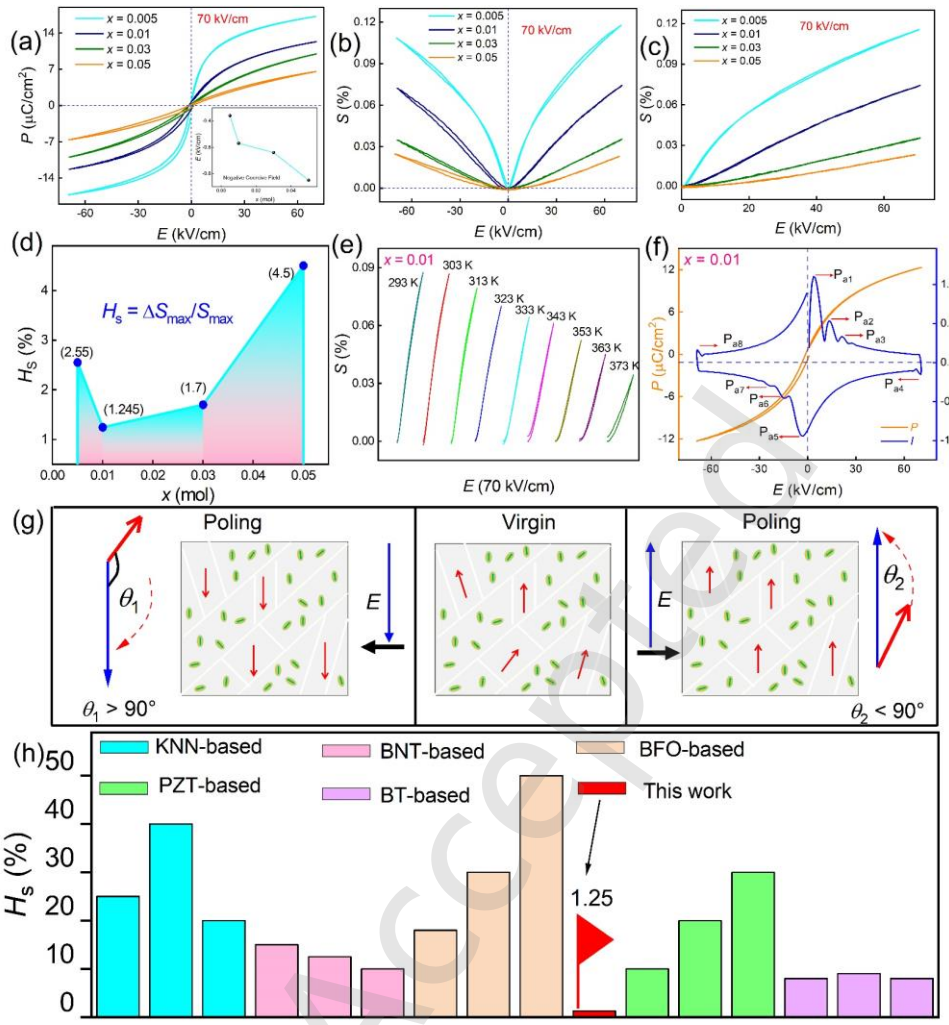

Fig. 2 (a) *P*–*E* hysteresis loops of $B_{(1-x)}ST$–*x*Sb ceramics at 70 kV/cm. (b) bipolar *S*–*E* hysteresis loops. (c) unipolar *S*–*E* hysteresis loops. (d) H_s of $B_{(1-x)}ST$–*x*Sb ceramics. (e) temperature-dependent *S*–*E* curves for the *x* = 0.01. (f) *I*–*E* and *P*–*E* curves for the *x* = 0.01. (g) schematic illustration of different domain deflection angles during the repolarization process. (h) comparison of H_s with other ceramic materials [20, 26, 32–43].

All samples exhibit narrow *P*–*E* and strain–electric field intensity (*S*–*E*) hysteresis loops, and the loops measured under positive electric fields are slimmer than those under negative electric fields, as shown in Figs. 2(a) and 2(b) and Fig. S1. It can be observed in the inset of Fig. 2(a) that the positive coercive field is approximately zero,

whereas a distinct negative coercive field is observed, indicating that the built-in electric field (E_i) is successfully established after aging treatment due to introduction of defects. Through the XPS spectral in Fig. S14, we confirmed that the defects are indeed induced by A-site Ba vacancies and B-site Sb acceptor doping. This phenomenon is attributed to the defect dipoles polarization along with the spontaneous polarization direction after aging, resulting in the asymmetry $P-E$ and $S-E$ hysteresis loops [24].

Figs. 2(c−d), Figs. S2 and S5 show the H_s of ceramics with different x, and the H_s decreases initially and then increases, and the near-zero H_s (~1.25%) is achieved at x = 0.01. Compared with the undoped composition, the H_s decreases dramatically from 33.48% to below 4%. Moreover, as illustrated in Fig. 2(h), the H_s value of our ceramic is markedly lower than those of perovskite lead-free ceramics and commercial lead-based PZT ceramics, demonstrating its distinct advantage. This ultra-low H_s is associated with the HAG-PNRs and multiphase coexistence, which can weaken energy barrier for polar regions switching and provide multiple polar directions [25]. Since the HAG-PNRs are located above the temperature of the maximum dielectric peak (T_m) at room temperature, the ceramics reside in a non-freezing, coexisting glassy state. These HAG-PNRs respond rapidly to external electric fields, thereby avoiding the effects typically induced by domain switching and domain wall motion.

Fig. 2(e) shows the temperature-dependent $S-E$ curves of the $B_{(1-x)}ST-x$Sb ceramic, and the S performance initially remains constant and then gradually decreases with increasing temperature. Generally, as the temperature exceeds T_m, the activity of PNRs

gradually decreases. As the temperature approaches the Burns temperature (T_B), the PNRs gradually fade, causing the S to decrease [26, 27]. However, after the temperature exceeds the Burns temperature (313 K), the S of the material does not drop abruptly. It should be attributed to the synergistic effect of defect dipoles and the built-in electric field in the composition [28−31]. As clearly shown in Fig. S6, even when the measurement temperature exceeds T_B, the ferroelectric P–E loop persists, and the bipolar strain S–E curve still retains its asymmetric shape—thicker on the left and thinner on the right. This further confirms that the strain performance, which does not drop abruptly above T_B, is indeed dominated by the defect complexes formed by defect dipoles.

When the applied electric field (E) is parallel to E_i, the effective field E_{eff} is the sum of E and E_i, providing a great driving force for polar regions switching [40]. Meanwhile, most defect dipoles are already oriented at a small angle relative to spontaneous polarization under the applied field, thereby reducing the required rotation angle for polar regions [26], as shown in Fig. 2(g). The combined effect of the increased effective field and the favorable initial dipole alignment leads to easier domain switching, resulting in the observed slim ferroelectric/S loop at positive electric field, while E_i weakens the external electric field at negative electric field direction, resulting in a fat ferroelectric/S [44], namely, a broader left branch and a narrower right branch. Accordingly, near-zero H_s of ~1.25% is observed under a positive electric field. This finding is further corroborated by the corresponding I−E curves presented in Fig. 2(f) and Fig. S7. As shown in Fig. 2(f), eight distinct sharp peaks (P_{a1}−P_{a8}) are discernible

in the *I–E* curve, each corresponding to a separate current jump associated with a distinct physical origin. Among these current peaks, the P_{a1} peak exhibits the sharpest and most intense current surge, originating from the nearly zero positive coercive field and the built-in electric field. Under these conditions, the effective electric field rapidly exceeds the coercive field, triggering the switching of a large number of HAG-PNRs with extremely low switching barriers, thereby generating the highest current peak. P_{a2} peak emerges as the electric field increases, reflecting the gradual switching of inert PNRs (I-PNRs) that possess higher reorientation energy barriers. P_{a3} is attributed to the reorientation of defect dipoles that exhibit the highest energy barriers. These PNRs act as a "lubricant" for domain motion, facilitating the switching of domains and thereby markedly reducing the H_s. A sharp minor peak (P_{a4}) appears in the fourth quadrant, which arises from the recovery of a fraction of small domains/PNRs toward their original orientations under the defect-induced built-in field. As the positive field is gradually reduced, domains tend to reorient under built-in electric field, gradually increasing the current. Under negative electric field, large-scale domains reorient, producing another high-current peak (P_{a5}). P_{a6} and P_{a7} peaks follow mechanisms analogous to those of P_{a2} and P_{a3} peak, respectively. Their lower current density, compared with P_{a2} and P_{a3} peaks, stems from the larger reorientation angles θ2 (See Fig. 2(g)) and higher energy barriers of polar regions switching due to defects pinning, and P_{a8} peak shares an identical formation mechanism with P_{a4} [19, 45, 46].

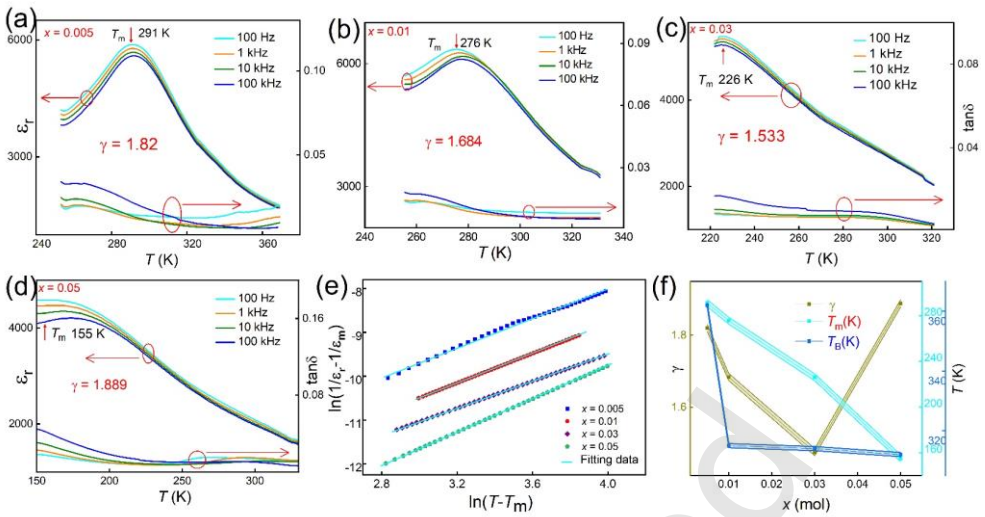

Fig. 3 (a−d) Temperature-dependent dielectric spectra of $B_{(1-x)}ST-xSb$ ceramics. (e) fitting of the diffuseness parameter (γ). (f) variation of γ, T_m, and T_B for various $B_{(1-x)}ST-xSb$ ceramic compositions.

The temperature dependence of the dielectric constant and loss for the $B_{(1-x)}ST-xSb$ ceramics is shown in Figs. 3(a)−5(d). Notably, the temperature (T_m) corresponding to the maximum dielectric constant decreases gradually with increasing Sb^{3+} content, indicating that the introduction of Sb^{3+} ions has decreased the phase transition temperature from the ferroelectric to the paraelectric phase. Furthermore, with increasing frequency, T_m shifts to higher temperatures and the dielectric peak broadens progressively, confirming that the partial long-range ferroelectric order in the $B_{(1-x)}ST-xSb$ compositions has been disrupted, resulting in the formation of a large number of PNRs [47, 48]. This phenomenon mainly originates from compositional fluctuations, lattice distortion, and the formation of defect dipoles induced by A-site Ba vacancies and B-site Sb^{3+} acceptor doping, lattice distortion and the formation of defect dipoles [31]. The relaxor behavior was quantitatively analyzed using the dispersion

factor (γ), which was determined by fitting the relationship between $\ln(1/\varepsilon_r - 1/\varepsilon_m)$ and $\ln(T - T_m)$. As shown in Fig. 3(e), Fig. S8, Fig. S10 and Fig. S17, the fitted relaxor factor (γ), T_m below room temperature, and the presence of abundant PNRs collectively confirm that all compositions are in a non-frozen ferroelectric glassy state, in which the long-range ferroelectric order is severely disrupted. In addition, as shown in the Fig 3(f) and Fig. S7, the T_B decreases gradually with the increase in Sb^{3+} contents and the T_B is 315 K at $x = 0.01$. Notably, the maximum T_m is below room temperature, indicating that the electrical properties measured above T_m, where the compositions possess a large number HAG-PNRs. Even when it is higher than T_B, at which polar regions are completely inactive. This proves that the electric properties indeed originate from defect dipoles beyond T_B.

Fig. 4(a) shows the XRD patterns of the $B_{(1-x)}ST-xSb$ samples, confirming the successful synthesis of a pure perovskite structure is successfully obtained. Moreover, Fig. 4(b) clearly shows that the magnified XRD patterns near 45° shift toward low angles, which is attributed to the substitution of larger-radius Sb^{3+} (76 pm) for smaller-radius Ti^{4+} (60.5 pm) or Sn^{4+} (69 pm), demonstrating the successful occupation of Sb ions at the B-site. Fig. 4(c) shows the fitted XRD peaks near 45°, revealing the coexistence of $(002)_T$, $(200)_R$, and $(002)_C$, as shown in Fig. 4(c). To systematically investigate the crystal structure, the XRD patterns of the ceramic samples were refined using GSAS−II software, as shown in Fig. 4(d) and Fig. S11. The experimental data are fitted to the coexistence of R, T, and C phase, and the low *wR* and *GOF* values indicate good agreement between the calculated and experimental data. Multiphase coexistence

not only reduces the domain switching barrier but also promotes rapid polarization alignment under an electric field, effectively mitigating H_s [21, 32, 49]. To investigate the phase structure change of the samples during temperature variations, variable-temperature XRD data were collected for x = 0.01, as shown in Fig. 4(e) and Fig. S12. The diffraction peaks near 45° and 56° remain unchanged, indicating that the ceramic sample at x = 0.01 exhibit no phase transition, Therefore, the weakening activity in polar regions (domain and PNRs) during heating is likely responsible for the fading S rather than phase transition.

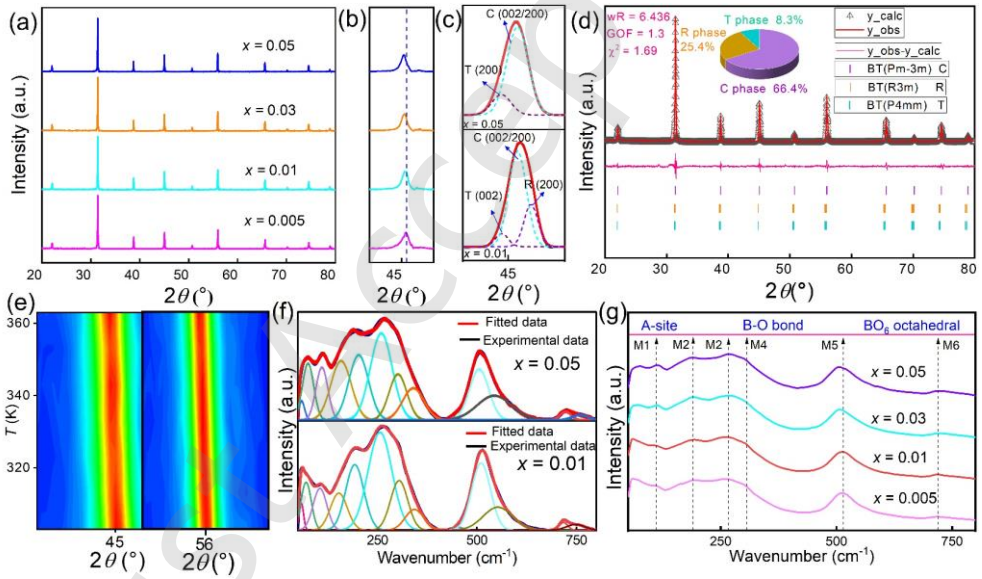

Fig. 4 (a) XRD patterns of $B_{(1-x)}ST-xSb$ ceramics. (b) magnified XRD patterns near 45°. (c) fitted XRD patterns near 45° for x = 0.01 and 0.05. (d) Rietveld refinement of the XRD pattern at x = 0.01. (e) temperature-dependent XRD patterns near 46° and 55° at x = 0.01. (f) deconvoluted Raman spectra for the x = 0.01 and 0.05. g Raman spectra of $B_{(1-x)}ST-xSb$ ceramics.

Raman spectroscopy was performed to further investigate the local structure evolution of the $B_{(1-x)}ST-xSb$ ceramics, as shown in Figs. 4(f) and 4(g). The spectra at x = 0.01 and x = 0.05 are deconvoluted using Gaussian-Lorentzian functions, revealing

13 distinct vibrational modes. Based on the characteristic vibration modes, the Raman spectra were categorized into three distinct regions. Region I (≤ 200 cm^{-1}) corresponds to the vibrations of A-site cations (Ba−O); Region II (200−400 cm^{-1}) is assigned to the vibrations of B-site cations (Sn/Ti/Sb−O); Region III (≥ 400 cm^{-1}) originates from the stretching/bending modes of the BO_6 oxygen octahedra. With increasing Sb^{3+} contents, all Raman peaks undergo significant broadening, indicating a weakening long-range ferroelectric order and an increase in structural disorder, thereby facilitating the formation of PNRs. Moreover, peaks in regions I and III shift toward lower wavenumbers, and weakening of the A−O bond and BO_6 octahedral bond strengths leads to lattice softening, which is attributed to the defect dipoles and lattice distortions induced by acceptor doping, further confirming the quenching of the long-range ferroelectric order and stabilization of a pseudo-cubic phase [50].

The SEM images in Fig. S15 show the surface morphology of the $B_{(1-x)}ST-xSb$ samples, sintered ceramics exhibit a dense microstructure with fine grains. With increasing Sb^{3+} doping, the grain size exhibits a non-monotonic trend, decreasing initially and then increasing, with the smallest grain size observed at x = 0.01. The synergistic effect of fine grains, optimally concentrated defect dipoles, and multiphase coexistence gives rise to HAG-PNRs, enabling the composition with x = 0.01 to achieve the lowest H_s [51].

To investigate the HAG-PNRs, the local domain structure of $B_{(1-x)}ST-xSb$ ceramics (x = 0.01 and 0.05) was characterized using in situ PFM. As shown in Figs. 5(a)−5(d), both samples exhibit a diffuse, patch-like domain morphology without sharp boundaries,

characteristic of non-frozen ferroelectric glass. Notably, the sample with x = 0.01 exhibits stronger piezoelectric active regions and a higher density of weak piezo-response regions (namely, HAG-PNRs) compared to x = 0.05 (Figs. 5(a) and 5(c)). This facilitates a rapid response to applied electric fields, promoting S while significantly reducing H_s [52, 53]. In contrast, the sample with higher defect concentration (x = 0.05) displays an even finer domain structure, composed of dispersed patch-like nanodomains (Figs. 5(b) and 5(d)). This refinement is attributed to increased lattice disorder induced by the higher defect density. To further explore the switching behavior, the polar regions were subjected to different voltages (10−40 V), as shown in Figs. 5(e)−5(l) and Fig. S16. Many polar regions in the x = 0.05 sample fail to switch even under 40 V, indicating the presence of inert polar regions, which results in inferior electric-field-induced S. Conversely, the polar regions at x = 0.01 switch more readily than those at x = 0.05 (Figs. 5(e)−5(h) and Figs. S16(a)−S16(d)), yielding higher S [23, 54]. Additionally, the polar regions at x = 0.01 revert to their initial state more easily than those at x = 0.05 (Figs. 5(i)−5(l) and Figs. S16(e)−S16(h)), which is conducive to reducing H_s.

Microstructure characterization and phase analysis of the $B_{(1-x)}ST-xSb$ materials were conducted using TEM, as shown in Figs. 5(m)−5(o). Based on the SAED patterns indexed using Gatan Digital Micrograph™ software, Fig. 5(m) reveals a tetragonal (*P*4*mm*) phase along the [110] zone axis. Correspondingly, Fig. 5(n) shows the FFT diffraction spots, consistent with a rhombohedral (*R*3*m*) phase along the [111] zone axis. Additionally, diffuse scattering rings are observed, indicative of the paraelectric cubic

($Pm\bar{3}m$) phase with short-range disorder [55]. These results align well with the Rietveld refinement of the XRD patterns at x = 0.01. Multiphase coexistence further reduces the domain switching barrier, facilitates domain reorientation, and suppresses H_s. Fig. 5(o) and Figs. S17(a)−S17(c) present high-resolution images of the domain structure, revealing numerous uneven protrusions characteristic of nanodomains. Defect-induced local regions disrupt the long-range ferroelectric order and generate HAG-PNRs, leading to an ultra-low H_s [56, 57].

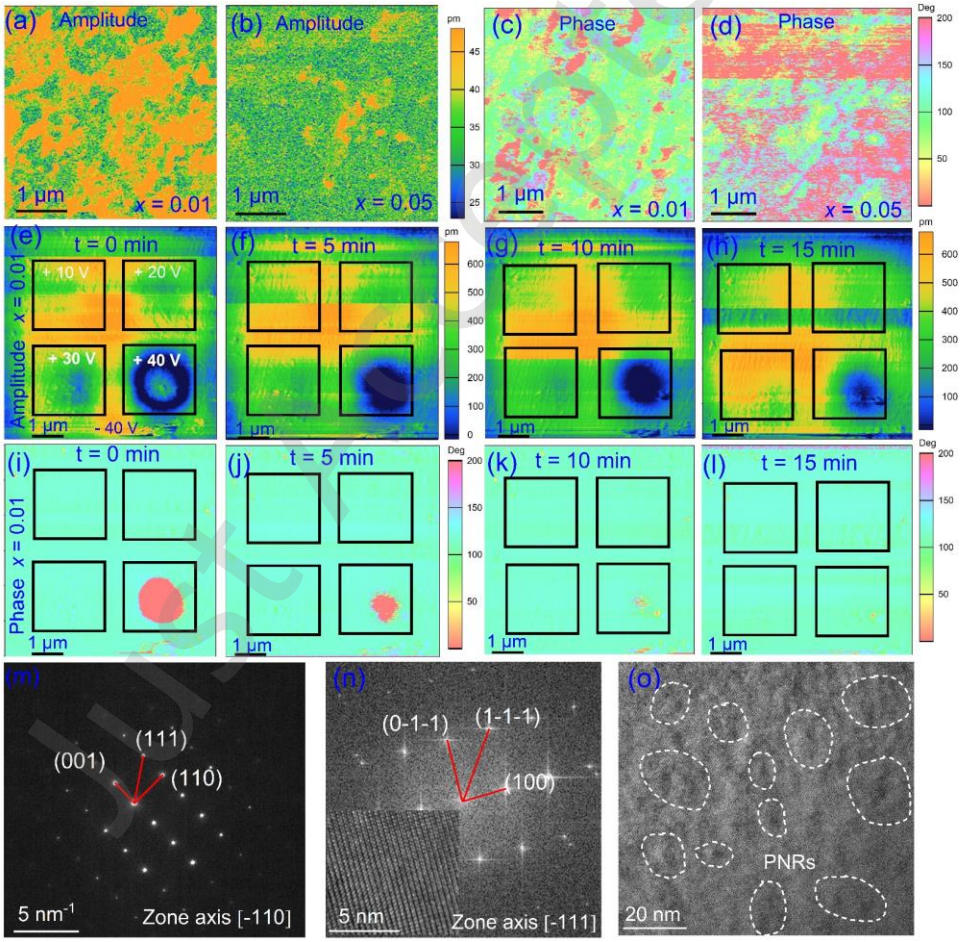

Fig. 5 (a−d) PFM amplitude and phase images for x = 0.01 and x = 0.05. (e−l) time-dependent evolution of domain-written amplitude and phase for x = 0.01 under an electric field (0, 5, 10, and 15 min). (m−o) selected area electron diffraction (SAED) patterns, fast Fourier transform (FFT)

patterns, and high-resolution domain structures for $x = 0.01$.

4. Conclusions

Through precise design of defect concentration to construct a non-freezing glassy state of HAG-PNRs, $B_{(1-x)}ST-xSb$ ceramics with near-zero H_s (~1.25%) have been successfully fabricated. By introducing Sb^{3+} at the B-site, acceptor doping not only creates defect dipoles that establish an internal built-in electric field, but also disrupts the long-range ferroelectric order, leading to the formation of HAG-PNRs. This structure significantly reduces the energy barrier for domain switching, thereby lowering the H_s of the material. Additionally, engineering a triple-phase coexistence (R−T−C) structure further decreases the energy barrier for domain reorientation. The combination of these strategies successfully achieves near-zero H_s. These patchy nanodomain structures observed via PFM corroborate the formation of HAG-PNRs. Coexistence of multiple phases was confirmed by TEM and Rietveld refinement of X-ray diffraction (XRD) patterns. This work provides a revolutionary approach for the material design of high-performance, environmentally friendly actuators.

Funding

This study received fundings from the National Key Research and Development Plan (2022YFF0706500), Construction of Science and Technology Platform of Guiyang ([2023]7-3), Industry and Education Combination Innovation Platform of Intelligent Manufacturing and Graduate Joint Training Base at Guizhou University (2020-520000-83-01-324061), Guizhou Engineering Research Center for smart services (2203-

520102-04-04-298868), Guizhou Provincial Basic Research Program (Natural Science) (No. QKHJC-ZK-2023-266). National Natural Science Foundation of China (62163006, 61605153), 2025 Targeted Support Project of Guizhou Provincial Laboratory Research (Qiankehe Platform SSYS(2025) Major 003).

Author contributions

Fangfang Zeng: Writing – review & editing, Writing – original draft, Supervision, Project administration, Methodology, Funding acquisition, Data curation, Conceptualization. **Hongbo Li**: Writing – original draft, Validation, Visualization, Investigation, Formal analysis, Data curation. **Yuhan Luan**: Resources, Investigation, Data curation. **Rongchuan He**: Software, Investigation, Data curation. **Xudong Luo**: Visualization, Software, Datacuration. **Xu Li**: Data curation. **Xiaoqiang Song**: Data curation. **Qingquan Xiao**: Validation. **Li Zhang**: Resources. **Jiajun Ma**: Methodology. **An Xue**: Funding acquisition. **Guifen Fan**: Validation. **Dawei Wang**: Supervision, Resources, Methodology.

Availability of data and materials

The data are available from the corresponding author upon reasonable request.

Competing interests

The authors have no competing interests to declare that are relevant to the content of this article.

Electronic Supplementary Material

Supplementary material mentioned above is available in the online version of this article.

References

[1] Zheng T, Wu JG, Xiao DQ*, et al.* Recent development in lead-free perovskite piezoelectric bulk materials. *Prog Mater Sci* 2018, **98**: 552−624.

[2] Chen L, Liu H, Qi H*, et al.* High-electromechanical performance for high-power piezoelectric applications: fundamental, progress, and perspective. *Prog Mater Sci* 2022, **127**: 100944.

[3] Nie PC, Li FZ, Ke H*, et al.* Advances in piezoelectric properties of textured ferroelectric ceramics with perovskite structure. *Advanced Ceramics* 2025, **46**: 171−194.

[4] Yang Y, Zhang QL, Zhang F*, et al.* Textured (K,Na)NbO_3 ceramics with enhanced piezoelectric properties: High k_p , d_{33} , and Curie temperature. *J Adv Ceram* 2025, **15**: 9221206.

[5] Ye F, Cheng H, Jiang XP*, et al.* Sn and Ce co-doping regulate phase structure of $NaNbO_3$: Double hysteresis loop and electro-strain. *J Adv Ceram* 2025, **14**: 9221119.

[6] Zeng FF, Liu QB, Cai EP*, et al.* Relaxor phenomenon of $(1-x)(Ba_{0.85}Ca_{0.15})(Zr_{0.09}Ti_{0.91})O_3-x$Ta + 0.6 wt% Li_2CO_3 ceramics with high piezoelectric

constant and Curie temperature. *Ceram Int* 2018, **44**: 10677−10684.

[7] Zeng FF, Liu QB, Peng SQ*, et al.* The (1−*x*)$Ba_{0.85}Ca_{0.15}Zr_{0.08}Ti_{0.92}$−*x*Ge lead-free ceramics with high piezoelectric activity and ultrahigh dielectric constant. *Ceram Int* 2019, **45**: 1416−1419.

[8] He HZ, Lv YT, Luan SW*, et al.* Enhancing the reliability of Dy-doped $BaTiO_3$ ceramics via grain boundary defect engineering. *Advanced Ceramics* 2026, **47**: 150−163.

[9] Yang Y, Ying L, Wang D*, et al.* High-performance lead-free ceramics with simultaneously high piezoelectricity and high mechanical quality factor. *Adv Mater* 2025, **37**: 202419325.

[10] Wang DW, Fan ZM, Rao GH*, et al.* Ultrahigh piezoelectricity in lead-free piezoceramics by synergistic design. *Nano Energy* 2020, **76**: 104944.

[11] Wang DW, Khesro A, Murakami S*, et al.* Temperature dependent, large electromechanical strain in Nd-doped $BiFeO_3$−$BaTiO_3$ lead-free ceramics. *J Eur Ceram Soc* 2017, **37**: 1857−1860.

[12] Qin HL, Zhao JW, Chen XX*, et al.* Investigation of lead-free $BiFeO_3$−$BaTiO_3$ piezoelectric ceramics through precise composition control. *J Adv Dielectr* 2023, **13**: 2350018.

[13] Qin HL, Zhao JW, Chen XX*, et al.* Investigation of $BiFeO_3$−$BaTiO_3$ lead-free piezoelectric ceramics with nonstoichiometric bismuth. *Microstructures* 2023, **3**: 2023035.

[14] Zhao JW, Qin HL, Chen XX*, et al.* Enhanced piezoelectric properties and electrical

resistivity in $CaHfO_3$ modified $BiFeO_3$−$BaTiO_3$lead-free piezoceramics. *J Materiomics* 2024, **10**: 416−422.

[15] Yang C, Cen ZY, Chen XF*, et al.* Large piezoelectric strain under a low driving electric field in Sm^{3+}-doped $BaTiO_3$ lead-free piezoelectric ceramics. *J Mater Chem A* 2025, **13**: 41729−41733.

[16] Li X, Fu J, Yang Y*, et al.* Ultrahigh electrostrains of lead-free (Ba,Ca)(Ti,Zr)O_3 piezoelectric ceramics via defect engineering. *J Mater Sci* 2022, **57**: 10233−10241.

[17] Baraskar BG, Kambale RC, James AR*, et al.* Ferroelectric, piezoelectric and electrostrictive properties of Sn^{4+}-modified $Ba_{0.7}Ca_{0.3}TiO_3$ lead-free electroceramics. *J Am Ceram Soc* 2017, **100**: 5755−5765.

[18] Feng W, Luo BC, Bian SS*, et al.* Heterostrain-enabled ultrahigh electrostrain in lead-free piezoelectric. *Nat Commun* 2022, **13**: 5086.

[19] Wu JY, Zhang HB, Huang CH*, et al.* Ultrahigh field-induced strain in lead-free ceramics. *Nano Energy* 2020, **76**: 105037.

[20] Hao J, Li W, Zhai J*, et al.* Progress in high-strain perovskite piezoelectric ceramics. *Mater Sci Eng R: Rep* 2019, **135**: 1−57.

[21] He RC, Guo HT, Yao ZK*, et al.* Negligible-hysteresis piezoceramic achieved by multiphase assisting and domain configuration manipulating. *J Adv Ceram* 2025, **14**: 9221160.

[22] Ji YC, Wang D, Wang Y*, et al.* Ferroic glasses. *npj Computational Materials* 2017, **3**(43): 5308.

[23] He LQ, Wang D, Xu MJ*, et al.* Large electrostrain with nearly-vanished hysteresis

in eco-friendly perovskites by building coexistent glasses near quadruple point. *Nano Energy* 2021, **90**: 106519.

[24] Varade P, Pandey AH, Selvamani R*, et al.* Tuning structural, dielectric, and ferroelectric properties of BTO-based ceramics through dual-site substitution. *Mater Chem Phys* 2024, **319**: 129381.

[25] Das Adhikary G, Adukkadan A, Muleta GJ*, et al.* Longitudinal strain enhancement and bending deformations in piezoceramics. *Nature* 2025, **637**: 333−338.

[26] Deng AP, Wu JG. Optimized strain properties with small hysteresis in BNT-based ceramics with ergodic relaxor state. *J Eur Ceram Soc* 2021, **41**: 5147−5154.

[27] Li TY, Liu C, Shi P*, et al.* High-performance strain of lead-free relaxor-ferroelectric piezoceramics by the morphotropic phase boundary modification. *Adv Funct Mater* 2022, **32**: 202202307.

[28] Waqar M, Wu HJ, Chen JS*, et al.* Evolution from lead-based to lead-free piezoelectrics: engineering of lattices, domains, boundaries, and defects leading to giant response. *Adv Mater* 2021, **34**: 202106845.

[29] Wang J, Wang BQ, Zhang HJ*, et al.* Ultrahigh electrobending deformation in lead-free piezoelectric ceramics via defect concentration gradient design. *Adv Mater* 2024, **36**: 202404682.

[30] Yao FZ, Wang K, Jo W*, et al.* Diffused phase transition boosts thermal stability of high-performance lead-free piezoelectrics. *Adv Funct Mater* 2016, **26**: 1217−1224.

[31] Kong S, Kumar N, Checchia S*, et al.* Defect-driven structural distortions at the surface of relaxor ferroelectrics. *Adv Funct Mater* 2019, **29**: 201900344.

[32] Cen ZY, Cao FZ, Feng MY*, et al.* Simultaneously improving piezoelectric strain and temperature stability of KNN-based ceramics via defect design. *J Eur Ceram Soc* 2023, **43**: 939−946.

[33] Habib M, Tang L, Xue GL*, et al.* Design and development of a new lead-free $BiFeO_3$−$BaTiO_3$ quenched ceramics for high piezoelectric strain performance. *Chemical Engineering Journal* 2023, **473**: 145387.

[34] Jin L, Luo WT, Hou L*, et al.* High electric field-induced strain with ultra-low hysteresis and giant electrostrictive coefficient in barium strontium titanate lead-free ferroelectrics. *J Eur Ceram Soc* 2019, **39**: 295−304.

[35] Li XS, Fu J, Yang YH*, et al.* Ultrahigh electrostrains of lead-free (Ba,Ca)(Ti,Zr)O_3 piezoelectric ceramics via defect engineering. *J Mater Sci* 2022, **57**: 10233−10241.

[36] Liu YC, Zhang HJ, Shi WM*, et al.* Ultra-low strain hysteresis in $BaTiO_3$-based piezoelectric multilayer actuators via microstructural texture engineering. *J Materiomics* 2025, **11**: 100882.

[37] Wang J, Wang BQ, Geng HF*, et al.* Boosting Low-*E* electro-strain via high-electronegativity B-site substitution in lead-free $K_{0.5}Na_{0.5}NbO_3$-based ceramics. *Acta material* 2025, **282**: 120520.

[38] Wang XJ, Wang J, Geng WP*, et al.* Large electrical strain in lead-free $K_{0.5}Na_{0.5}NbO_3$-based ceramics by heterovalent doping. *J Materiomics* 2023, **9**: 959−970.

[39] Yao MH, Li B, Gao HX*, et al.* Giant Electrostrain in Lead-free $BiFeO_3$−$BaTiO_3$ Ceramics via High-Entropy Design. *ACS Nano* 2025, **19**: 42772−42782.

[40] Zeng FF, Yao ZK, Zhang QS*, et al.* Low hysteresis in composites ceramics achieved by building polarization field and restoring force. *Mater Des* 2024, **248**: 113458.

[41] Zhang AM, Man WC, Jing RY*, et al.* Aliovalent co-doping induces relaxor states with enhanced electrostrain in BNT−based ceramics. *J Materiomics* 2025, **12**: 101107.

[42] Peng W, Chang JL, Zhao JW*, et al.* Enhanced piezoelectric properties and thermal stability of $LiNbO_3$-modified PNN−PZT ceramics. *J Materiomics* 2024, **10**: 995−1003.

[43] O'malley CJ, Tang XY, Koval V*, et al.* Unveiling the mechanism of substitution-induced high piezoelectric performance in PLZT ceramics. *J Adv Ceram* 2025, **14**: 9221097.

[44] Zhao ZH, Dai YJ, Huang F. The formation and effect of defect dipoles in lead-free piezoelectric ceramics: A review. *Sustain Mater Technol* 2019, **20**: e00092.

[45] Zheng T, Wu JG. Perovskite $BiFeO_3$−$BaTiO_3$ ferroelectrics: engineering properties by domain evolution and thermal depolarization modification. *Adv Electron Mater* 2020, **6**.

[46] Dong GS, Lin XJ, Li Q*, et al.* BNT-based ceramics with large strain and low hysteresis over a wide temperature range. *J Mater Sci Technol* 2025, **236**: 95−103.

[47] Bootchanont A, Triamnak N, Rujirawat S*, et al.* Local structure and evolution of relaxor behavior in $BaTiO_3$−$Bi(Zn_{0.5}Ti_{0.5})O_3$ ceramics. *Ceram Int* 2014, **40**: 14555−14562.

[48] Hou LH, Zhou CR, Li QN*, et al.* Giant strain with ultra-low hysteresis by tailoring relaxor temperature and PNRs dynamic in BNT-based lead-free piezoelectric ceramics. *Ceram Int* 2022, **48**: 13125−13133.

[49] Li TY, Lou XJ, Ke XQ*, et al.* Giant strain with low hysteresis in A-site-deficient $(Bi_{0.5}Na_{0.5})TiO_3$-based lead-free piezoceramics. *Acta Mater* 2017, **128**: 337−344.

[50] Yang Y, Ji YC, Fang MX*, et al.* Morphotropic relaxor boundary in a relaxor system showing enhancement of electrostrain and dielectric permittivity. *Phys Rev Lett* 2019, **123**: 137601.

[51] Ghayour H, Abdellahi M. A brief review of the effect of grain size variation on the electrical properties of $BaTiO_3$-based ceramics. *Powder Technol* 2016, **292**: 84−93.

[52] Kathait GS, Panwar NS, Maini S. Dielectric, piezoelectric and energy storage properties of large grain $Ba_{1-x}Sr_xTiO_3$ (BST) ceramic system for $0.17 \leq x \leq 0.26$. *Mater Sci Eng B* 2023, **297**: 116786.

[53] Khan SA, Ahmed T, Park HW*, et al.* Effects of B-site and A/B-sites Codoping on lattice distortion and defect concentration for high electromechanical response of lead-free piezoelectrics. *Acta Mater* 2024, **278**: 120262.

[54] Yang Y, Li Y, Song YQ*, et al.* Lead-free trirelaxor ferroelectrics: high energy storage capacity in the paraelectric state and broad operating temperature range. *Adv Mater* 2025, **38**: 202509323.

[55] Liu JN, Zhang DY, Yan YX*, et al.* Piezoelectric ceramic hardening through defect distribution optimization in multicomponent systems. *Adv Funct Mater* 2024, **35**: 202413130.

[56] Zhang C, Zhou ZX, Tang ZM*, et al.* Effects of scandium oxide on domain structure, dielectric and ferroelectric properties of barium zirconate titanate ceramics. *J Alloys Compd* 2021, **889**: 161622.

[57] Shee C, Banerjee S, Alagirusamy R*, et al.* Deployment of piezoelectric transducers for diverse technical applications: A comprehensive review. *Results Eng* 2025, **25**: 103881.